On the role of local heating on cathode degradation during the oxygen reduction reaction in solid acid fuel cells

Maximilian Wagner[a†], Oliver Lorenz[a], Felix P. Lohmann-Richters[b], Aron Varga[c] and Bernd Abel[a]

[a]Leibniz Institute for Surface Engineering, Department of Functional Surfaces, Permoserstraße 15, 04318 Leipzig, Germany
[b]Forschungszentrum Jülich GmbH, Institut für Energie- und Klimaforschung - Elektrochemische Verfahrenstechnik (IEK-14), 52425 Jülich, Germany
[c]BMW Group, Department Electrical Drive Development, Taunusstraße 41, 80807 Munich, Germany
†maximilian.wagner@iom-leipzig.de, Tel.: +49 341 235 3365, Fax.: +49 341 235 2584

Keywords: solid acid fuel cell; intermediate temperature fuel cells; degradation; stability; oxygen reduction reaction

Abstract

Reliable, stable, and long-term performance is one of the most important requirements for fuel cells in general. Widespread application of intermediate temperature solid acid fuel cells is still hindered by relatively fast degradation. However, durability studies are both expensive as well as, by their nature, time consuming and therefore rarely performed. In this study, we propose a viable method to investigate degradation pathways on a practical time scale. Five different types of electrodes were fabricated with varying geometrical complexity, but all containing platinum as the electrocatalyst. By utilizing small amounts of well-connected platinum as electrode catalyst, outstanding mass normalized currents were achieved resulting in accelerated cell degradation. Clearly observable effects on the electrodes were characterized ex situ by scanning electron microscopy and the electrochemical activity measured in operando by the decline of the current density at a constant cell voltage. After electrochemical measurement, changes of the electrodes were almost exclusively limited to the cathode side, where the electrolyte CsH_2PO_4 penetrated the previously distinct platinum layer originating from the current collector fibers. The observed morphological changes decreased the number of electrocatalytically active sites by covering the platinum layer or isolating the current collectors. These effects correlate both with the duration of the measurement and the current density. At different potentials, an asymptotic behavior of the cell performance was observed, identifying current-induced localized heating as the main degradation mechanism. Due to the high overpotential at the cathode, hotspots close to the current collectors could reach sufficient temperatures during cell

operation to facilitate a morphological change of the electrolyte. This work gives a detailed analysis of the degradation mechanism in platinum-based solid acid fuel cell electrodes, providing valuable information for designing stable high-performance electrodes.

Broader Context

The strengthened global effort to decarbonize the electricity infrastructure by shifting to renewable energy sources is inevitably linked to the development of sufficient energy storage and transformation capabilities. Intermediate temperature fuel cells are a promising technology for a highly efficient, on-demand transformation of chemical into electrical energy. With an operating temperature-range of 230°C to 260°C, solid acid fuel cells are filling the temperature gap between high temperature polymer electrolyte membrane fuel cells (HT-PEM-FC) and solid oxide fuel cells. They combine resistance to poisoning with a high catalytic activity and good fuel flexibility. Solid acid fuel cells are already used in industry on a small scale, but the development has recently been hampered by the poor stability of the cathode electrode.[1] Relatively little is known about the degradation mechanism and the topic is addressed rarely in the field. In this work, a current density dependent, morphology change of CsH_2PO_4 is observed during operation. This marks the starting point for multiple deactivation and degradation processes. We demonstrated a general degradation mechanism for the most promising and widely investigated solid acid compound (CsH_2PO_4), allowing a wide range of further improvements leading towards stable, high performance intermediate temperature fuel cells.

Introduction

Since solid acid fuel cells (SAFC) were first introduced by Haile et al. in 2001, they received growing interest as an intermediate temperature fuel cell.[2] They work with a solid, non-toxic proton conducting electrolyte at operating temperatures of 230 °C – 260°C, allowing fuel flexibility and good catalytic activity while relatively cheap auxiliary components can be utilized.[2] In the last years, different solid acids ($M_xH_y(AO_4)_z$ M= K, Rb, Cs; A= S, Se, P) were investigated and CsH_2PO_4 (CDP) is generally accepted as the most promising compound.[2–6] At 228°C, CsH_2PO_4 undergoes a reversible

phase transition from a low temperature paraelectric phase into a high conductivity phase, increasing the proton conductivity by several orders of magnitude to about 0.02 S cm^{-1}. The transition is accompanied by an increase in the plasticity of CsH_2PO_4.[7] Humidification of the gas stream is essential to prevent dehydration into the favored metaphosphate phase.[8–11] In a temperature-range between 230°C and 260°C, the dehydration process from CsH_2PO_4 to solid $CsPO_3$ through a solid cesium hydrogen pyrophosphate ($CsH_2P_2O_7$) has been reported.[12] However, for temperatures exceeding 260°C in a humidified gas atmosphere, the formation of a liquid transient phase ($CsH_{2(1-x)}PO_{4-x}$) during the dehydration process was observed.[13] Therefore, temperatures exceeding the safe operating window of CsH_2PO_4 are detrimental for the long-term stability and cell performance. Especially the possible formation of a liquid phase during cell operation could present a major issue for the stability of any solid acid based fuel cell.

For so-called high temperature polymer electrolyte membrane fuel cells (HT-PEM-FC) the adsorption of phosphate to the platinum catalyst at the cathode in form of $H_2PO_4^-$ is a problematic and well investigated phenomenon.[14–19] HT-PEM-FCs operate at 120-200°C with membranes based on polybenzimidazole and/or pyridine polymers doped with concentrated and highly corrosive H_3PO_4.[20,21] Depending on the temperature and cell potential, phosphate adsorbs on the platinum surface at the cathode, blocking active sites.[14–16] A reduction from PO_4^{3-} to strongly adsorbing species such as PO_3^{3-} occurs at potentials below 0.48 V vs dynamic hydrogen electrode (DHE), resulting in catalyst poisoning.[17,22–25] Dissolution of platinum, by forming a platinum-phosphate complex was reported for potentials close to the open circuit voltage, either by direct dissolution of Pt or by the dissolution via PtO_x. [17,18,26] For SAFC, Lohmann-Richters et al. reported a very slow platinum dissolution process.[27] Since the fuel cells electrochemically analyzed in our study were neither held close to OCV for a longer time nor were subject to cyclic voltammetry experiments, dissolution processes are most likely not relevant for our experiments. Compared to phosphoric acid, CsH_2PO_4 is less corrosive and the phosphate anions are tied to the crystal structure as long as it remains in the solid state. If entering a liquid state however, a similar reaction as with phosphoric acid may occur at the platinum surface. Up

to now, local hotspots in SAFC electrodes, as they occur in solid oxide fuel cells, are suspected to be the dominant cause for electrode performance degradation, where solid to liquid phase transition of CsH_2PO_4 ultimately leads to a poisoning of the platinum catalyst surface.[28–31]

Platinum is most commonly used as electrode catalyst due to its high activity and stability.[32–34] Increasing the platinum utilization is a crucial part in the ongoing SAFC research.[35–37] At the electrode, the chemical reaction generally takes place at the so-called triple phase boundary (TPB) between the catalyst, the proton conducting electrolyte and the gas phase. For platinum thin film electrodes, Louie et al. reported a two-phase boundary mechanism for the anode side. There, hydrogen diffuses through the thin platinum layer to the platinum – electrolyte interface where the charge transfer reaction takes place. Whether the oxygen reduction reaction at a platinum thin film cathode can occur through a similar two-phase boundary process or only at the TPB, e.g. at microcracks in the catalyst surface, is still unknown.[38] Either way, both the electron conducting catalyst and the ion conducting electrolyte need to be fully interconnected to prevent isolated and therefore inactive domains. This represents a very complex and challenging system with multiple factors possibly limiting the reaction rate.[33] State-of-the-art cells work with porous electrodes to maximize the active site density, achieving platinum utilizations of 280 mW mg_{Pt}^{-1}.[37] Tada et al. reported the importance of the porosity to decrease mass flow over potentials.[35] However, in a previous study, we have shown a clear limit beyond which an increased porosity leads to an increased electrolyte resistance, limiting the cell performance.[39] While an optimization of the catalyst activity is crucial for the potential use of solid acid fuel cells, the long-term stability is at least as important and rarely addressed. Chisholm et al. reported degradation effects of the chemical and microstructural evolution limited to the cathode side. While the anode side remains as prepared, they observed a densification of the porous structure at the cathode.[7] Since stability experiments over thousands of hours -as required for industrial applications- are very challenging on a laboratory scale, a modified cell design is essential to measure and identify the degradation pathways. State-of-the-art powder electrodes provide a very complex three dimensional and relatively stable system. Simplifying this setup to an electrode consisting of a platinum thin film

layer of constant thickness applied on top of a CsH_2PO_4 pellet with known morphology provides a well-defined and easy to analyze cell. Such cells with low platinum loading (64 μg_{Pt} cm^{-2}) show remarkably high mass normalized current densities (up to 2300 mA mg_{Pt}^{-1} during I-V characterization experiments, ESI, S1) and sufficiently accelerated degradation during fuel cell operation, enabling us to investigate the degradation mechanism on a reasonable time scale. Taking this into consideration, these cells constitute model electrodes to analyze the degradation mechanisms and do not represent an optimized cell construction in terms of power output or current densities.

In the present work, we investigate the stability of different thin film electrodes for up to 70 h at fuel cell conditions and with accelerated degradation protocols. The stability as a function of the voltage was investigated by applying different cell voltages over 15 h, repeatedly interrupted by additional electrochemical characterization measurements. Scanning electron microscopy (SEM) images before and after electrochemical measurements were taken for both the anode and cathode and correlated with the observed performance decline.

Experimental section

Synthesis and fabrication of membrane electrode assemblies

The solid acid electrolyte CsH_2PO_4 was synthesized as previously described.[36] In brief, 25 g of H_3PO_4 (85 %, Carl Roth) was diluted with 80 ml of methanol (99.9 %, anhydrous, Alfa Aesar). A stoichiometric quantity of Cs_2CO_3 (99%, Alfa Aesar) was then dissolved in 300 ml of methanol and quickly added to the H_3PO_4-methanol mixture. The suspension was stirred for 20 minutes followed by filtration, washing and drying of the reaction product. The crystal structure of the product was confirmed by X-ray powder diffraction measurements. The as-synthesized CsH_2PO_4 powder was pressed with an automatic, uniaxial hydraulic press (GS25440-AtlasTM Automatic 15T) at 250 MPa for 5 minutes into dense polycrystalline electrolyte disks (20 mm in diameter, 1 mm in thickness). Solid acid fuel cells used in this work consist of a symmetric membrane electrode assembly (MEA) which is composed of a 1 mm thick, dense CsH_2PO_4 membrane and the same electrode type for anode and cathode, sandwiched between two electron collectors (see Table 1) and gas diffusion layers (PACOPOR ST 60 AL3, PACO Paul GmbH und Co. KG). Platinum was used as catalyst and applied by DC magnetron sputtering (Edwards Auto 306, 300W, 5 mTorr Ar). The deposited platinum amount, controlled by a quartz crystal micro balance measurement, was 64 $\mu g_{Pt}\ cm^{-2}$ per electrode for all MEAs. Five different MEAs were produced, denoted as CP/**Pt@CDP$_{porous}$**, CP/**Pt@CDP**, CP_{MPL}/**Pt@CDP**, **Pt@CP**/CDP and **Pt@CP$_{MPL}$**/CDP, Table 1. For clarity, the material on which the catalyst was applied is marked bold in the acronym.

Table 1 Specifics for the different MEAs. All were fabricated symmetrically with the same electrode type as anode and cathode and a constant platinum content of 64 µg/cm² per electrode.

MEA-Type	Electrochemical characterization	Electron collector	Electrode type	Number of analyzed cells
CP/**Pt@CDP$_{porous}$**	CstV, OCV, IVC, SPEIS	CP[a]	Pt deposition on porous CsH_2PO_4 layer	One for each analyzation time (2 h;10 h and 70 h)
CP/**Pt@CDP**	CstV, OCV, IVC, SPEIS[c]	CP[a]	Pt deposition on CsH_2PO_4 pellet	4 for each CstV (0.35 V; 0.50 V and 0.70 V)
CP_{MPL}/**Pt@CDP**	CstV, OCV, IVC, SPEIS	CP_{MPL}[b]	Pt deposition on CsH_2PO_4 pellet	4

Pt@CP/CDP	CstV, OCV, IVC, SPEIS	CP[a]	Pt deposition on CP	1
Pt@CP$_{MPL}$/CDP	CstV, OCV, IVC, SPEIS	CP$_{MPL}$[b]	Pt deposition on CP-MPL	3

[a] Carbon paper: Toray Inc. TGP-60. [b] Carbon paper: Toray Inc. TGP-H-60-MPL. [c] For CP/**Pt@CDP**, SPEIS was conducted only for CstV at 0.35 V. CstV: constant voltage, OCV: open circuit voltage, IVC: I-V characterization, SPEIS: staircase potential electrochemical impedance spectroscopy.

For the CP/**Pt@CDP$_{porous}$** MEA, a 15 µm thick porous layer was applied to a pressed CsH_2PO_4 pellet by a spray drying process prior to the platinum deposition via DC magnetron sputter deposition. For the spray drying process, a precursor solution consisting of CsH_2PO_4, methanol (99.9 %, Alfa Aesar), DI-water and polyvinylpyrrolidone (99%, PVP, 1,300,000 g mol^{-1}, Alfa Aesar) was aerosolized by a piezoelectric spray head resulting in particles with the size between 100 nm to 5 µm (ESI, S2). A detailed description of the cell preparation and the spraying process was reported earlier.[39] The CP/**Pt@CDP** and CP$_{MPL}$/**Pt@CDP**-MEA are reproductions of the platinum thin film cells based on the work Louie et al. with a sputter deposited platinum layer on a polished, dense CsH_2PO_4 pellet.[38] They differ only in the respective carbon paper, see Table 1. For **Pt@CP**/CDP and **Pt@CP$_{MPL}$**/CDP, platinum was sputtered on the respective carbon paper surface, which were subsequently placed on both sides of a polished CsH_2PO_4 pellet.

Electrochemical characterization

Electrochemical data was recorded with a Biologic VSP 300 potentiostat with the cells held at 240°C in a humidified (0.4 atm H_2O) gas flow of 75 sccm for both oxygen and hydrogen. The reactions at the anode side are much faster and the anode was used as a pseudo reference electrode for all voltages given in this report.[6,40] This configuration has been used before in several publications.[27,41–43] An harsh accelerated degradation protocol, utilized previously by Lohmann-Richters et al. for SAFC, was used in this work.[27] CP/**Pt@CDP**-MEAs were cycled at 0.5 V s^{-1} for 4000 cycles each, first between 0.6 V and 1.5 V and then between 0.05 V and 1.5 V.[27,44] These measurements were not used to characterize the electrochemical properties of the electrodes but to cause accelerated degradation effects at the electrodes to be analyzed by SEM. For electrochemical characterization, the MEAs given

in Table 1 were subjected to a repeated two step testing protocol. 1.) Characterization including open circuit voltage (OCV), staircase potential electrochemical impedance spectroscopy (SPEIS) with a 10 mV perturbation amplitude over a frequency range of 1 kHz to 100 mHz at voltages of 0.05 V and 0.35 V as well as I-V characterization from OCV to 0 V with a scan rate of 10 mV s^{-1} followed by 2.) Current density measurement at a constant cell voltage (CstV) of either 0.35 V, 0.5 V or 0.7 V for a certain time. The external resistance, resulting from wires and electrical contacts is an order of magnitude lower than the electrolyte resistance and can be neglected. The electrolyte resistance, used to calculate I-R corrected IVC curves, is obtained from the high frequency intercept of the real axis. The averaged open circuit voltage of all cells was 0.91±0.03 V with no significant time dependency (OCV for each MEA in ESI, S3). To analyze the stability as a function of voltage, CP/**Pt@CDP**-MEAs were held at a CstV of either 0.35 V, 0.5 V and 0.7 V (Table 1). IVC curves were repeatedly recorded for comparison. The current density at 0.35 V (after I-R correction) from these IVC measurements was plotted vs. time to compare the different conditions. This enables us to compare the activity at 0.35 V while the cells remained at the respective voltages for over 99% of the measurement time. The reference voltage of 0.35 V was representative, the same trends would occur for other voltages. The mass normalized current density is the ratio of the current density and the platinum content of 64 µg cm^{-2}.

Characterization

The electrode morphology was characterized using scanning electron microscopy (Ultra 55 SEM, Carl Zeiss Ltd.) with a secondary electron (SE) detector for the topographical analysis and an electron back scatter (BSE) detector or angular back scatter (AsB) detector for the differentiation between CsH_2PO_4, carbon and platinum. If not stated otherwise, images were recorded with a secondary electron detector using an acceleration voltage of 5 keV. BSE images were taken with an acceleration voltage of 2 keV and AsB images with 25 keV. X-ray diffraction experiments to control the purity of the CsH_2PO_4 after synthesis were realized on a G670 Guinier Camera (Huber) using copper K_α radiation (λ = 1.541 Å) and a 2Θ-range between 15° and 70° (ESI, S4).

Results and discussion

MEAs investigated in this work showed a fast decrease of the current density during constant voltage measurements associated with clear morphological changes of the electrodes. This becomes particularly obvious for CP/**Pt@CDP$_{porous}$** where platinum is applied on top of a porous CsH_2PO_4 layer. Figure 1 shows the time-dependent activity decrease during constant voltage measurements. Over the course of 70 h, the initial current density is decreased to 25 % of its starting value. Within the first hours, an exponential decline of the current density was recorded, followed by gradual stabilization of the cell performance. Three cells were measured and removed after reaching 80 % (2 h), 40 % (10 h) and 25 % (70 h) of the initial current density respectively and the cathode surfaces investigated by SEM imaging.

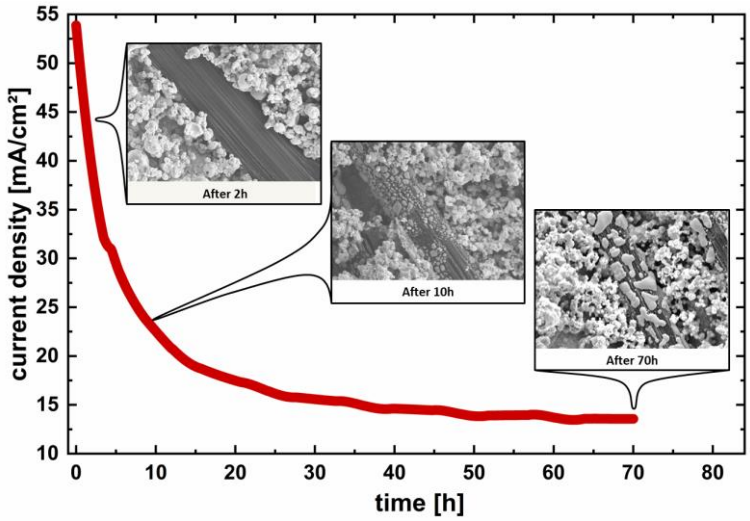

Figure 1 A representative plot of the current density as a function of time, taken at 0.35 V for the CP/**Pt@CDP$_{porous}$**-MEA. The insets show representative ex situ electron micrographs of the porous cathode after 2 h, 10 h and 70 h respectively.

The electrode morphology is largely intact after 2 h of testing and platinum is homogenously covering the porous CsH_2PO_4 structure. After measuring for 10 h, agglomeration of the CsH_2PO_4 was observed originating from the carbon fibers, where small, round particles of CsH_2PO_4 appeared. After 70 h, when the cell reached a stable performance, most of the porous structure close to the carbon fiber was agglomerated. SEM images showed a clear change in the electrode surface localized around the carbon

fiber current collectors while the structure further away from the current collector showed small or no signs of morphological changes. The observed morphological changes were not limited to the CP/**Pt@CDP**$_{porous}$-MEA. Before electrochemical testing, CP/**Pt@CDP**-MEAs had a continuous and uniform catalyst layer over the pressed electrolyte pellet with CsH_2PO_4 grain boundaries visible because of the topological contrast, Figure 2 (a).

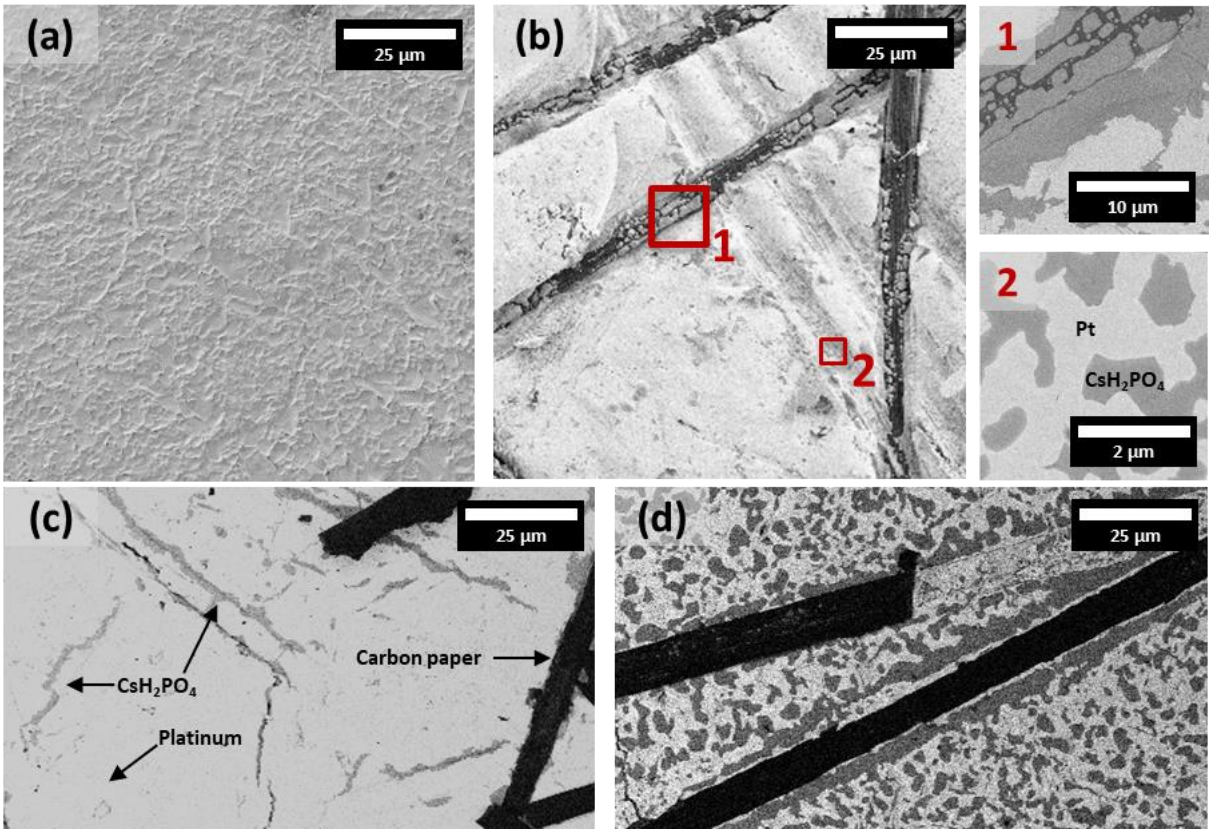

Figure 2 Scanning electron micrographs of a CP/**Pt@CDP**-MEA cathode (a) before and (b) after a 15 h electrochemical measurement with CstV at 0.35 V. Before the measurement (a), platinum forms a homogenous layer. After the measurements however (b), loose carbon fibers or their imprints are visible as well as a penetration of the previously homogenous platinum layer by CsH_2PO_4, especially close to the fibers. The insets (1,2) magnify two particular areas showing the disruption by CsH_2PO_4 using a back-scattering detector to visualize element differences. With this detector, carbon appears black, while platinum appears light grey and CsH_2PO_4 dark grey. After the accelerated degradation protocol (c), back scattering images of the anode side show only minor changes in the platinum surface. However, the catalyst layer of the cathode side (d) is severely damaged, especially close to the current collector fibers.

The appearance of the cathode surface changed significantly after constant voltage measurements (b): Carbon fibers and their imprints can be observed as well as CsH_2PO_4 agglomerations on the carbon fibers and around the imprints. The insets 1 and 2 show high magnification images obtained via a back-scattering electron (BSE) detector to differentiate between carbon fibers (black), CsH_2PO_4 (dark grey) and platinum (light grey). CsH_2PO_4 is partially covering the carbon fibers and almost no platinum can be detected around these strands, which can be seen particularly clearly in inset 1. When focusing on a carbon fiber imprint (inset 2), the previously homogenous platinum layer is interrupted by areas where CsH_2PO_4 is visible on the surface. The areas where the platinum layer is disrupted, CsH_2PO_4 does not show the typical grain edges but developed rounded shapes as occurring for solidified liquids. After thin film electrodes were subject to an accelerated degradation protocol, differences of the anode and cathode sides were investigated by SEM, Figure 2. While the anode side (c) showed few disruptions of the platinum layer and these only very close to carbon fibers, the cathode (d) developed significant surface changes. While the platinum layer here is disrupted over the whole sample, almost no platinum is visible close to the carbon fibers. Since CsH_2PO_4 acts as an insulator for electrons, this leads to an interruption of the contact between the current collector and the platinum surface and certain areas of the platinum surface can be isolated from the current collector. The limitation of the degradation effect to the cathode side is in agreement with literature and presumably caused by heat generated due to the high overpotential of the oxygen reduction reaction (ORR).[7,45] The severe damage through the accelerated degradation protocol may increased by a platinum dissolution process known for HT-PEM-FC. [17,18,26]

An interesting observation can be made via the AsB detector with high accelerating voltages and hence large sampling depth. While areas of CsH_2PO_4 formed at the surface during measurements, we found evidence of the platinum thin film underneath the CsH_2PO_4. Having a closer look at the areas where CsH_2PO_4 is present at the surface, it emerged through the platinum layer and agglomerated on top as partially connected spots, Figure 3 (top view (a) and side view (b)).

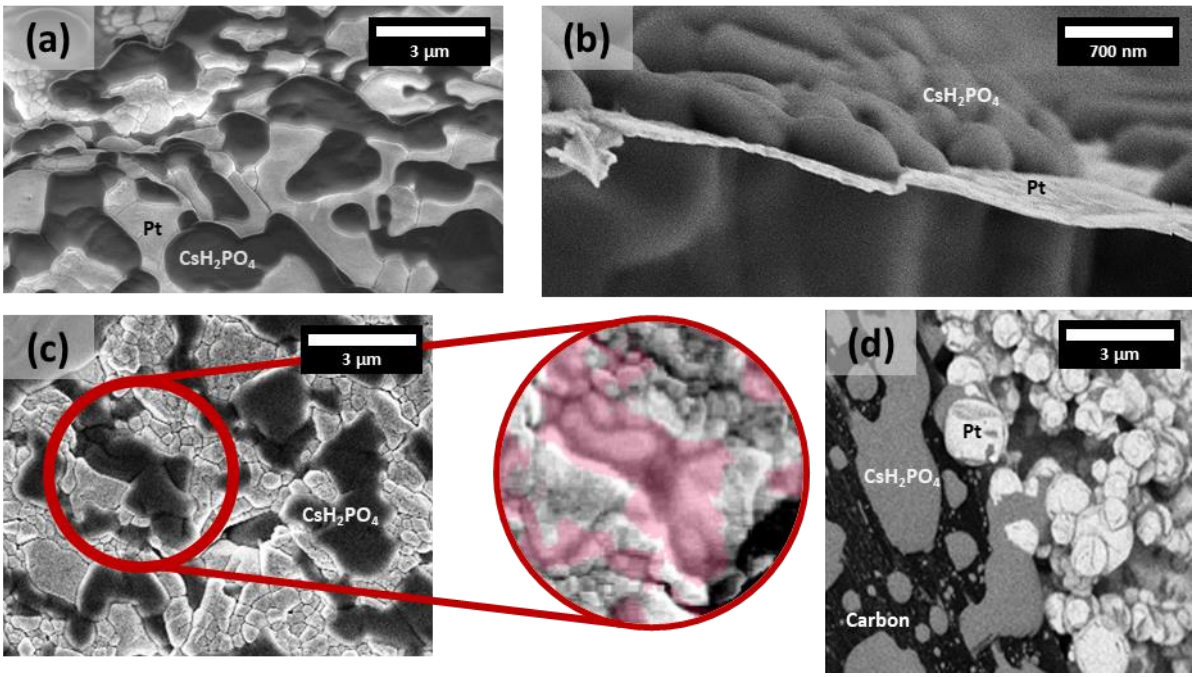

Figure 3 Representative SEM micrographs of the cathode surface with all relevant phases labelled. After an accelerated degradation protocol: (a) Top view and (b) cross section of the catalyst layer penetrated by CsH_2PO_4. (c) Top view of the CP/**Pt@CDP**-MEA partially covered by CsH_2PO_4, the magnification represents an overlay with an AsB detector image revealing the underlying platinum film. After constant voltage measurement: (d) Agglomeration of CsH_2PO_4 particles close to the current collector on a CP/**Pt@CDP**$_{porous}$ cathode. During the agglomeration process platinum vanishes from the particle surface.

With an AsB detector, the underlying platinum structure can be detected through the electrolyte on top. The enlarged section of Figure 3 (c) shows an overlay of the secondary electron micrograph of the cathode surface with an AsB image. CsH_2PO_4 was colored pink in order to highlight the boundaries of the platinum layer. The CsH_2PO_4 seems to creep through the platinum layer, covering the nearby area without destroying the existing platinum layer. Even though the platinum layer still exists underneath, the connection to gas phase is lost, preventing further reactions. Figure **3**(d) shows the BSE image of a CP/**Pt@CDP**$_{porous}$ cathode close to a carbon fiber taken after a 70 h constant voltage measurement discussed in Figure 1. The light grey platinum can easily be distinguished from the darker CsH_2PO_4. On the carbon fiber, most CsH_2PO_4 already agglomerated. In the center of the image (d), the agglomeration process is captured: Most of the CsH_2PO_4 has already lost its initial polycrystal

morphology and no platinum can be detected on the surface of these regions. In total, it may be that during the morphological changes of CsH_2PO_4, the platinum is covered by the CsH_2PO_4 and cannot be reached by the gaseous reactants anymore. Throughout this process, the active platinum surface decreases and an isolating CsH_2PO_4 zone forms around the current collectors, causing the observed decline in electrode performance.

For the time-dependent evolution of the current density shown in Figure 4 (a), CP/**Pt@CDP**-MEAs were held at a constant voltage of 0.7 V (black), 0.5 V (red) and 0.35 V (blue). After certain time steps, IVC measurements were taken for each cell to compare their performance at equal voltages. Each data point presented in Figure 4 (b) corresponds to the current density at 0.35 V during IVC. Due to the short acquisition time for the IVC measurement, the cell remained over 99 % of the time at the given constant voltage.

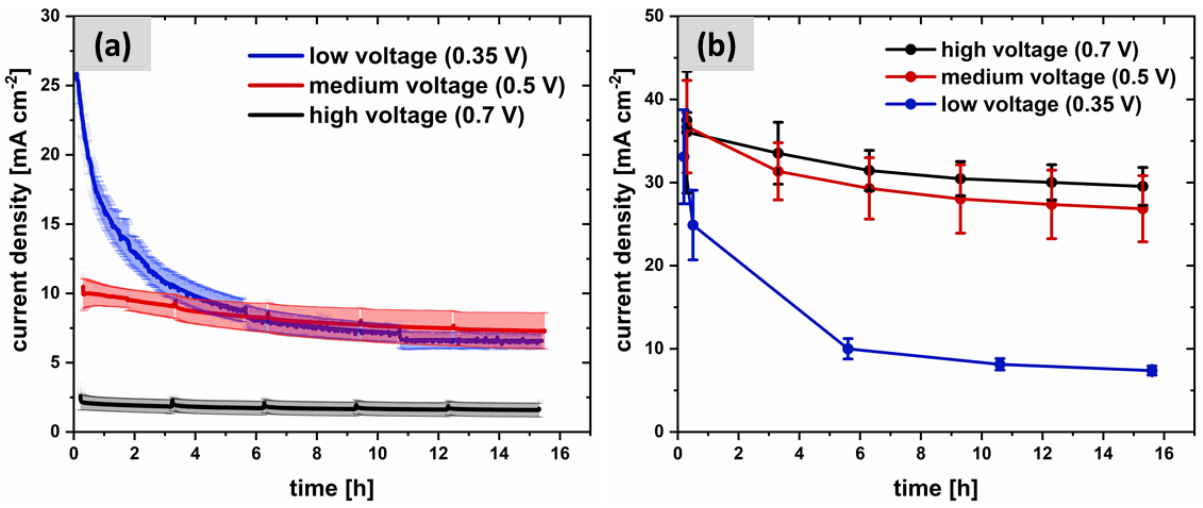

Figure 4 (a) Current density of CP/**Pt@CDP**-MEA cells over time at three different cell voltages: 0.7 V (black), 0.5 V (red) and 0.35 V (blue). To compare the activity under the same conditions, the measurements in (a) were regularly interrupted by IVC measurements. Each data point shown in (b) represents the current density corresponding to a I-R corrected voltage of 0.35 V, allowing a direct comparison of the stability.

At a cell voltage of U = 0.7 V, a low initial current density was generated (2.3 ± 0.7 mA cm^{-2}) and at U = 0.5 V a medium initial current density of 10.1 ± 1.3 mA cm^{-2} was measured. High initial current densities of 25.9 ± 1.6 mA cm^{-2} occurred at a voltage of U= 0.35V. We denote these as 'high', 'medium' and 'low voltage conditions' respectively. Cells under low voltage conditions showed an asymptotic

behavior of the current over time. After a fast and reproducible decline of the activity within the first four to six hours, both the current density and speed of degradation converged with the performance of the cells under medium voltage condition. Cells under high and medium voltage conditions showed only a minor decrease over time, presenting in turn a major improvement in stability. The differences in degradation rate caused by the high and medium voltage conditions are thereby very low, even though the respective current densities vary significantly. These measurements verify the current density as a major factor in the degradation mechanism of solid acid electrodes. The density of the current has a nonlinear influence on the degradation, as observed in the activity decline under low voltage conditions. Since the effects of this process are only visible at the cathode, we propose a temperature induced degradation mechanism, Figure 8. Due to the high overpotential at the cathode side, most waste heat is generated at the cathodic active sites during the reaction.[7,45] Under operating conditions, a liquid phase transition for CsH_2PO_4 was reported starting at 280°C.[13] This requires a marked increase in local temperature and the occurrences of such hot-spots are very difficult to prove directly. Even when not reaching the phase transition temperature, CsH_2PO_4 in its super protonic phase develops a high plasticity, which could facilitate the observed creep at elevated temperatures.[7] This would require a high temperature dependency of the plasticity, which is unknown at present. Once the electrolyte is in the liquid or high plasticity state, different degradation mechanisms can occur: 1. The platinum catalyst is covered by CsH_2PO_4 resulting in a decrease of active sites due to a gas supply disruption. 2. Changes in the CsH_2PO_4 morphology causing an interruption of the connection between the platinum layer and current collector, inactivating large areas of the electrode. 3. Catalyst poisoning occurs due to adsorption of $H_2PO_4^-$ on the platinum surface from the liquid state CsH_2PO_4. This process is well known for HT-PEM-FC working with phosphoric acid at temperatures between 120°C -200°C. Even though phosphate adsorption has not been analyzed for CsH_2PO_4 so far, its occurrence is likely since adsorption was reported for the given potential range and the same anion species ($H_2PO_4^-$) is present in the liquid transition phase of CsH_2PO_4.[13,14] The respective impact of these processes is

difficult to estimate but all result from a current density/heat induced morphological change of the CsH_2PO_4.

A Nyquist representation of SPEIS measurement at 0.05 V for the CP/**Pt@CDP**-MEA during CstV at 0.35 V is shown in Figure 5. Typical features include the electrolyte resistance obtained from the high frequency x-axes intersection, the charge transfer resistance of the electrodes and the inductive behavior at low frequencies.

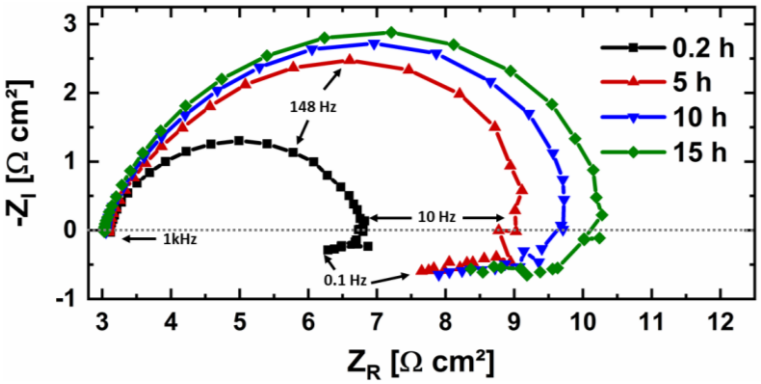

Figure 5 Representative SPEIS at 0.05 V for the CP/**Pt@CDP**-MEA during CstV at 0.35 V. Selected frequencies are marked for orientation.

While the electrolyte resistance remained stable, the charge transfer resistance increased during the measurement, which agrees with the observed decline in performance. The same tendency can be seen for the other MEA types (ESI, S5). Even though the interpretation of the impedance data must be treated carefully since no steady state was reached due to the ongoing degradation, some interesting conclusion can be drawn. The semicircle symmetry in Figure 5 is depressed, indicating either the involvement of more than one faradaic reaction or topological influences like a heterogenous current distribution. If the latter is the case, the Impedance data is influenced by a distributed time constant and can be described by a constant phase element (CPE). In general, time constant distribution can result from geometry induced non-uniform currents, electrode porosity or parasitic reactions. [46–48]. For simple faradaic reaction without diffusion, the impedance can be expressed in terms of a constant phase element as given in Equation 1. Following abbreviations are used: R_e: electrolyte resistance, R_{CT}: charge transfer resistant, j: imaginary number √ (-1), α and Q: CPE specific parameters.

$$Z(\omega) = R_e + \frac{R_{CT}}{1 + (j\omega)^{\alpha} Q R_{CT}} \qquad \text{Equation 1}$$

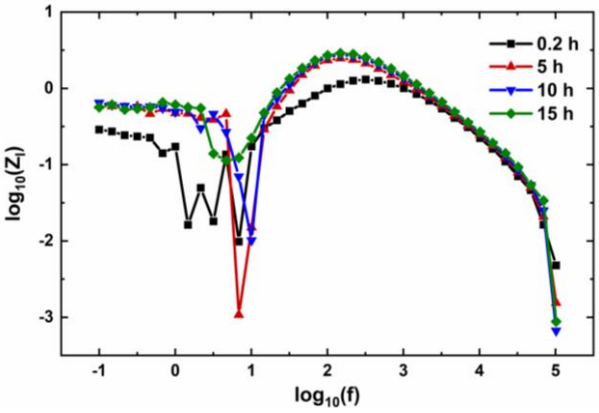

Figure 6 Imaginary part of the impedance plotted against the frequency on a logarithmic scale. CPE exponent "α" was obtained by fitting between 4.72 kHz and 21.9 kHz. The distortion of the symmetry gives an indication of more than one reactive process.

When plotting the imaginary part of the impedance against the frequency on a logarithmic scale (Figure 6), the constant phase element exponent "α" can be obtained by fitting the slope in the high frequency region, Table 2.

Table 2 Analysis of the slope between 4.72 kHz and 21.9 kHz in the log(Z_I) vs log(f) representation

Slope between 4.72 kHz and 21.9 kHz				
time	0.2 h	5 h	10 h	15 h
α	0,859±0.028	0,824±0.023	0,839±0.017	0,814±0.009
R	0.9957	0.9968	0.9984	0.9996

Departure from α= -1 indicates a CPE behavior for the high frequency region with a distributed time constant instead of multiple discrete ones. The lack of symmetry suggest that the high frequency capacitance is in parallel to other reactive processes.[49] While the presented data is unsuited for an equivalent circuit based fitting procedure, the slight change of the α value over time indicates a change in the electrode morphology as observed ex situ by SEM imaging. A low frequency inductive loop is seen below 10 Hz. Roy et al. discussed similar inductive loops to be attributed to processes occurring in PEM fuel cells and associated them with degrading side reactions such as PtO_x formation and

platinum dissolution.[50,51] The results in Figure 5 indicate a side reaction such as catalyst poisoning but interpretation of the low frequency domain should be treated carefully, since the same observations can be caused by non-stationary effects such as changes of the surface topology. Based on the significant morphological changes observed via SEM it can't conclusively be clarified by the presented data whether a side reaction such as PtO_x formation or phosphate contamination is responsible for the observed low frequency behavior.

In Figure 7 the time-dependent evolution of the current density for four different MEA types is shown. For CP/**Pt@CDP** and CP_{MPL}/**Pt@CDP,** the platinum covered CsH_2PO_4 surface is contacted with the respective carbon paper as current collector. CP_{MPL}/**Pt@CDP** shows a higher initial current density as well as a slower decrease with the time. The micro porous carbon paper provides a larger contact area resulting in a more homogeneous current distribution, which indicates a limiting effect of the in-plane conductivity of the platinum thin film. Despite the slightly higher stability, the same morphological changes can be seen exclusively at the cathode (ESI, S6).

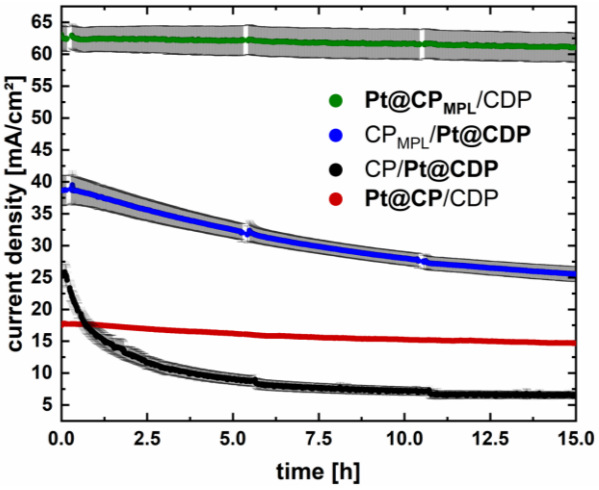

Figure 7 Comparison of the current density of CP/**Pt@CDP**, Pt/**CP**, CP_{MPL}/**Pt@CDP** and **Pt@**CP_{MPL}/CDP-MEA at 0.35V over time. Gaps in the measurements are caused by additional characterization measurements (SPEIS, OCV, IVC).

For **Pt@CP**/CDP and **Pt@**CP_{MPL}/CDP-MEA the catalyst was applied directly on the respective carbon paper and active sites can only be present at the contact area between the platinum covered carbon

paper and the CsH_2PO_4 surface. Both MEAs have a good stability during the measurement time and especially the **Pt@CP$_{MPL}$**/CDP-MEAs show a remarkable current density, which can be explained by the larger contact area of the CP_{MPL}, resulting in a higher density of well-connected electrochemically active sites. SEM images of the **Pt@CP**/CDP-MEA show a similar morphological change of the electrolyte as reported for other MEA types around the carbon fibers, however, an undamaged platinum layer was observed where the carbon fibers were detached from the surface (ESI, S7 and S8). The higher stability seems be caused by the better attachment of catalyst to the current collector, since platinum was applied directly to the current collector. CsH_2PO_4 does not penetrate the platinum surface and does not cause an interruption of the catalyst-current collector connection. The electrode is therefore less effected by the morphology change of the electrolyte which results in a higher stability. SEM measurements for the **Pt@CP**/CDP MEA reveal a contact area between the carbon paper and electrolyte surface of about 18 ± 9 % (ESI, S9). Similar investigations for the **Pt@CP$_{MPL}$**/CDP-MEA were not possible because the micro porous layer stuck to the electrolyte surface after electrochemical analysis and could not be removed. The initial current density at 0.35 V of the **Pt@CP**/CDP MEA, however, is only 30 % lower compared to CP/**Pt@CDP,** where the whole CsH_2PO_4 surface is in contact with the catalyst. This indicates that most of the reaction is taking place very close to the carbon fibers and areas further away from the current collectors only provide a small fraction of the total current density. The connection of remote areas to the carbon fibers is based exclusively on the conduction through the platinum thin film. For a 30 nm thick film, bulk resistivity can be assumed, resulting in a sheet resistance of 6.6 Ω at 240°C, which may increase further during heat up due to crack formation in the catalyst layer (ESI, S10).[52] In summary, a high ohmic resistance between remote areas and the current collector can explain their small contribution. Consequently, high current densities are generated merely in close proximity to the carbon fibers during fuel cell operation. Because of the cathodic overpotential, the produced waste heat initiates the formation of critical hot-spots around the carbon fibers at which the temperature rise causes an agglomeration of the electrolyte as seen in Figure 2 and Figure 3. This concept is illustrated in Figure 8.

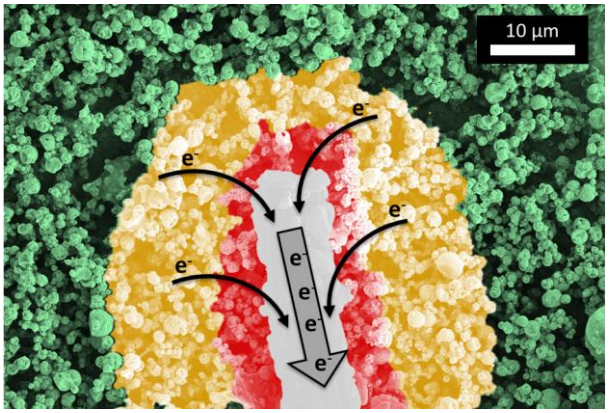

Figure 8 Illustration of a temperature induced degradation mechanism. Areas very close to the current collector fibers develop a very high current densities, causing the local temperature to increase at the cathode due to the high overpotential of the oxygen reduction reaction. At some local hot-spots this leads to a phase transition of the CsH_2PO_4 into a liquid state or increased plasticity, which causes a decrease of active sites and ultimately results in a decreased cell activity.

During constant voltage measurements, agglomeration of CsH_2PO_4 disable highly active areas close to the current collector. More remote areas have a lower activity and do not generate sufficient waste heat to cause the temperature induced degradation. After a certain time, critical hot-spots become inactive and the cell performance stabilizes at a reduced current density. This effect can be seen in Figure 4, where the current density of the low voltage condition (blue curve) rapidly decreases within the first four to six hours. After that time, it reached values similar to the medium voltage condition. The stability of the low voltage condition after this point (6 h) resembles the course of the medium and high voltage condition, indicating the absence of critical hot-spots. In general, uniform heat distribution and local current densities on the cathode are identified as important aspects for improving the long-term stability. In our work, improvements were achieved by using micro porous current collectors as well as direct application of the catalyst to the current collector. Based on the presented data, promising strategies to further stabilize the performance include: 1. Reducing the overpotential of the oxygen reduction reaction by using improved catalyst for instance platinum alloys. Such alloys already showed promising results for intermediate fuel cells and could reduce the generated waste heat at a given cell performance.[53–55] 2. Alloys can also increase the tolerance against

phosphate poisoning. For HT-PEM-FC a binder coated PtNiCu catalyst demonstrated a good resistance to poisoning.[56] 3. Improving the thermal stability of CsH_2PO_4 by mixing with different additives. Various combinations enhancing CsH_2PO_4 properties have already been discovered.[10,57–59]

Conclusion

The long-term stability of solid acid fuel cells with low platinum loadings was investigated in this study with the aim to identify the main degradation pathways. The cells were designed for accelerated degradation in order to study the degradation mechanism during constant voltage measurements on a reasonable time scale. The key point was the utilization of small but well-connected platinum amounts as electrode catalyst, resulting in very high currents per mg_{Pt}. SEM images as well as constant voltage measurements showed a time and current density dependent agglomeration of CsH_2PO_4 especially close to the current collector fibers. During this process, platinum is removed from the electrolyte surface or is covered by CsH_2PO_4 creeping through microcracks of the catalyst layer, resulting in fewer active sites and partially isolated current collectors. Additionally, Impedance measurements indicate that a catalyst poisoning for example due to phosphate adsorption may occur. The respective contributions to the overall degradation are difficult to analyze but are all based on the observed morphological change of CsH_2PO_4. In agreement with the literature, visible effects were largely limited to the cathode side and likely correlated to the waste heat generated by the cathodic overpotential during operation.[7] A nonlinear dependency of the current density was found. While cells with a current density below 10 mA cm^{-1} (medium and high voltage conditions) showed a very slow performance decline, asymptotic behavior occurred while currents exceeded this value. With decreasing current densities, fewer critical local hotspots are generated and performance stabilization begins. Whether the generated heat is sufficient to initiate a phase transition into a liquid transient state or just increase the plasticity of the electrolyte could not be conclusively clarified. Overall, the current density and through this, the locally generated heat was identified as the main degradation

cause. Increasing the density of the current collectors by micro porous layer had a beneficial effect on the stability especially when the catalyst was directly applied to the current collector.

Based on this work, heat distribution and local current density over the cathode should be considered a key element when construction long-term stable solid acid fuel cells. Presented information provides the basis for further improvements by 1. Finding new catalyst alloys to further reduce the ORR overpotential 2. Discovering phosphate poisoning resistant alloys 3. Improving the thermal stability of CsH_2PO_4 by mixing with different additives. In summary, this paper gives an insight into the degradation mechanism of solid acid fuel cell electrodes. It presents an effective analysis method for long term stability, indicates the main degradation causes and provides a guideline to further improve the long-term stability of solid acid fuel cells.

References

[1] Nasa Spinoff, *Versatile Fuel Cells Stop Natural Gas Emissions at Oil Wells*, https://spinoff.nasa.gov/Spinoff2020/ee_5.html.

[2] Haile, S. M.; Boysen, D. A.; Chisholm, C. R.; Merle, R. B., *Nature*, (2001) **410**, 910.

[3] Boysen, D. A.; Uda, T.; Chisholm, C. R. I.; Haile, S. M., *Science (New York, N.Y.)*, (2004) **303**, 68.

[4] Goñi-Urtiaga, A.; Presvytes, D.; Scott, K., *International Journal of Hydrogen Energy*, (2012) **37**, 3358.

[5] Paschos, O.; Kunze, J.; Stimming, U.; Maglia, F., *Journal of physics. Condensed matter : an Institute of Physics journal*, (2011) **23**, 234110.

[6] Haile, S. M.; Chisholm, C. R. I.; Sasaki, K.; Boysen, D. A.; Uda, T., *Faraday discussions*, (2007) **134**, 17-39; discussion 103-18, 415-9.

[7] Calum R.I. Chisholm, Dane A. Boysen, Alex B. Papandrew, Strahinja Zecevic, SukYal Cha, *The Electrochemical Society Interface*, (2009), 53.

[8] Louie, M. W.; Kislitsyn, M.; Bhattacharya, K.; Haile, S. M., *Solid State Ionics*, (2010) **181**, 173.

[9] Baranov, A. I.; Khiznichenko, V. P.; Sandler, V. A.; Shuvalov, L. A., *Ferroelectrics*, (1988) **81**, 183.

[10] Otomo, J., *Solid State Ionics*, (2003) **156**, 357.

[11] Haile, S. M.; Liu, H.; Secco, R. A., *Chem. Mater.*, (2003) **15**, 727.

[12] Taninouchi, Y.-k.; Uda, T.; Awakura, Y.; Ikeda, A.; Haile, S. M., *J. Mater. Chem.*, (2007) **17**, 3182.

[13] Taninouchi, Y.-k.; Uda, T.; Awakura, Y., *Solid State Ionics*, (2008) **178**, 1648.

[14] Kaserer, S.; Caldwell, K. M.; Ramaker, D. E.; Roth, C., *Journal of Physical Chemistry C*, (2013) **117**, 6210.

[15] Nart, F. C.; Iwasita, T., *Electrochimica Acta*, (1992) **37**, 385.

[16] Habib, M. A., *J. Electrochem. Soc.*, (1985) **132**, 108.

[17] Prokop, M.; Kodym, R.; Bystron, T.; Drakselova, M.; Paidar, M.; Bouzek, K., *Electrochimica Acta*, (2020) **333**.

[18] Prokop, M.; Kodym, R.; Bystron, T.; Paidar, M.; Bouzek, K., *Electrochimica Acta*, (2019) **313**, 352.

[19] Park, H.-Y.; Ahn, S. H.; Kim, S.-K.; Kim, H.-J.; Henkensmeier, D.; Kim, J. Y.; Yoo, S. J.; Jang, J. H., *Journal of the Electrochemical Society*, (2016) **163**, F210-F215.

[20] Li, Q.; Jensen, J. O.; Savinell, R. F.; Bjerrum, N. J., *Progress in Polymer Science*, (2009) **34**, 449.

[21] Zhang, J.; Xie, Z.; Zhang, J.; Tang, Y.; Song, C.; Navessin, T.; Shi, Z.; Song, D.; Wang, H.; Wilkinson, D. P.; Liu, Z.-S.; Holdcroft, S., *Journal of Power Sources*, (2006) **160**, 872.

[22] Sugishima, N., *J. Electrochem. Soc.*, (1994) **141**, 3325.

[23] Sugishima, N., *J. Electrochem. Soc.*, (1994) **141**, 3332.

[24] Prokop, M.; Bystron, T.; Bouzek, K., *Electrochimica Acta*, (2015) **160**, 214.

[25] Prokop, M.; Bystron, T.; Paidar, M.; Bouzek, K., *Electrochimica Acta*, (2016) **212**, 465.

[26] Bindra, P., *J. Electrochem. Soc.*, (1979) **126**, 1631.

[27] Lohmann-Richters, F. P.; Abel, B.; Varga, Á., *J. Mater. Chem. A*, (2018) **6**, 2700.

[28] Mangold, M.; Krasnyk, M.; Sundmacher, K., *Chemical Engineering Science*, (2004) **59**, 4869.

[29] Kim, S. J.; Choi, M.-B.; Park, M.; Kim, H.; Son, J.-W.; Lee, J.-H.; Kim, B.-K.; Lee, H.-W.; Kim, S.-G.; Yoon, K. J., *Journal of Power Sources*, (2017) **360**, 284.

[30] Bavarian, M.; Soroush, M.; Kevrekidis, I. G.; Benziger, J. B., *Ind. Eng. Chem. Res.*, (2010) **49**, 7922.

[31] Ju, G.; Reifsnider, K.; Huang, X., *Journal of Fuel Cell Science and Technology*, (2008) **5**.

[32] Qing, G.; Kikuchi, R.; Takagaki, A.; Sugawara, T.; Oyama, S. T., *Electrochimica Acta*, (2015) **169**, 219.

[33] Lohmann, F. P.; Schulze, P. S. C.; Wagner, M.; Naumov, O.; Lotnyk, A.; Abel, B.; Varga, Á., *J. Mater. Chem. A*, (2017) **5**, 15021.
[34] Papandrew, A. B.; St. John, S.; Elgammal, R. A.; Wilson, D. L.; Atkinson, R. W.; Lawton, J. S.; Arruda, T. M.; Zawodzinski, T. A., *J. Electrochem. Soc.*, (2016) **163**, F464-F469.
[35] Tada, S.; Tajima, S.; Fujiwara, N.; Kikuchi, R., *International Journal of Hydrogen Energy*, (2019) **44**, 26545.
[36] Suryaprakash, R. C.; Lohmann, F. P.; Wagner, M.; Abel, B.; Varga, A., *Rsc Advances*, (2014) **4**, 60429.
[37] Papandrew, A. B.; Chisholm, C. R. I.; Elgammal, R. A.; Özer, M. M.; Zecevic, S. K., *Chem. Mater.*, (2011) **23**, 1659.
[38] Louie, M. W.; Haile, S. M., *Energy Environ. Sci.*, (2011) **4**, 4230.
[39] Wagner, M.; Dreßler, C.; Lohmann-Richters, F. P.; Hanus, K.; Sebastiani, D.; Varga, A.; Abel, B., *J. Mater. Chem. A*, (2019) **7**, 27367.
[40] Sasaki, K. A.; Hao, Y.; Haile, S. M., *Physical Chemistry Chemical Physics*, (2009) **11**, 8349.
[41] Shetzline, J. A.; Bukola, S.; Creager, S. E., *Journal of Electroanalytical Chemistry*, (2017) **797**, 8.
[42] Torija, S.; Prieto-Sanchez, L.; Ashton, S. J., *Journal of Power Sources*, (2016) **327**, 543.
[43] Brightman, E.; Hinds, G.; O'Malley, R., *Journal of Power Sources*, (2013) **242**, 244.
[44] Pizzutilo, E.; Geiger, S.; Grote, J.-P.; Mingers, A.; Mayrhofer, K. J. J.; Arenz, M.; Cherevko, S., *J. Electrochem. Soc.*, (2016) **163**, F1510-F1514.
[45] Unnikrishnan, A.; Rajalakshmi, N.; Janardhanan, V. M., *Electrochimica Acta*, (2018) **261**, 436.
[46] Jurczakowski, R.; Hitz, C.; Lasia, A., *Journal of Electroanalytical Chemistry*, (2004) **572**, 355.
[47] Lukács, Z., *Journal of Electroanalytical Chemistry*, (1999) **464**, 68.
[48] Lukács, Z., *Journal of Electroanalytical Chemistry*, (1997) **432**, 79.
[49] Orazem, M. E.; Pébère, N.; Tribollet, B., *J. Electrochem. Soc.*, (2006) **153**, B129.
[50] Roy, S. K.; Orazem, M. E., *J. Electrochem. Soc.*, (2007) **154**, B883.
[51] Roy, S. K.; Orazem, M. E.; Tribollet, B., *J. Electrochem. Soc.*, (2007) **154**, B1378.
[52] Avrekh, M.; Monteiro, O.R.; Brown, I.G., *Applied Surface Science*, (2000) **158**, 217.
[53] Paik, H.; Berenov, A. V.; Skinner, S. J.; Haile, S. M., *APL Materials*, (2019) **7**, 13201.
[54] Rao, C. V.; Parrondo, J.; Ghatty, S. L.; Rambabu, B., *Journal of Power Sources*, (2010) **195**, 3425.
[55] Mamlouk, M.; Jang, J. H.; Scott, K., *Journal of Fuel Cell Science and Technology*, (2012) **9**.
[56] Park, H.; Kim, D.-K.; Kim, H.; Oh, S.; Jung, W. S.; Kim, S.-K., *Applied Surface Science*, (2020) **510**.
[57] Muroyama, H.; Matsui, T.; Kikuchi, R.; Eguchi, K., *Journal of Physical Chemistry C*, (2008) **112**, 15532.
[58] Matsui, T.; Kukino, T.; Kikuchi, R.; Eguchi, K., *J. Electrochem. Soc.*, (2006) **153**, A339.
[59] PONOMAREVA, V.; SHUTOVA, E., *Solid State Ionics*, (2007) **178**, 729.